



Soft x-ray microscopy with 7 nm resolution

BENEDIKT RÖSNER,^{1,*} SIMONE FINIZIO,¹ FRIEDER KOCH,¹ FLORIAN DÖRING,¹
 VITALIY A. GUZENKO,¹ MANUEL LANGER,¹ EUGENIE KIRK,^{1,2} BENJAMIN WATTS,¹
 MARKUS MEYER,³ JOSHUA LOROÑA ORNELAS,³ ANDREAS SPÄTH,³ STEFAN STANESCU,⁴
 SUFAL SWARAJ,⁴ RACHID BELKHOU,⁴ TAKASHI ISHIKAWA,¹ THOMAS F. KELLER,^{5,6} BORIS GROSS,⁷
 MARTINO POGGIO,⁷ RAINER H. FINK,³ JÖRG RAABE,¹ ARMIN KLEIBERT,¹ AND CHRISTIAN DAVID¹

¹Paul Scherrer Institut, 5232 Villigen PSI, Switzerland

²Laboratory for Mesoscopic Systems, Department of Materials, ETH Zürich, 8093 Zürich, Switzerland

³Department of Chemistry and Pharmacy, FAU Erlangen-Nürnberg, Egerlandstr. 3, 91058 Erlangen, Germany

⁴Synchrotron SOLEIL, L'ormes des Merisiers, Saint Aubin BP-48, 91192, Gif-Sur-Yvette Cedex, France

⁵DESY NanoLab, Notkestr. 85, 22607 Hamburg, Germany

⁶Physics Department, Hamburg University, 20355 Hamburg, Germany

⁷Department of Physics, University of Basel, 4056 Basel, Switzerland

*Corresponding author: benedikt.roesner@psi.ch

Received 9 June 2020; revised 29 September 2020; accepted 4 October 2020 (Doc. ID 399885); published 10 November 2020

The availability of intense soft x-ray beams with tunable energy and polarization has pushed the development of highly sensitive, element-specific, and noninvasive microscopy techniques to investigate condensed matter with high spatial and temporal resolution. The short wavelengths of soft x-rays promise to reach spatial resolutions in the deep single-digit nanometer regime, providing unprecedented access to magnetic phenomena at fundamental length scales. Despite considerable efforts in soft x-ray microscopy techniques, a two-dimensional resolution of 10 nm has not yet been surpassed in direct imaging. Here, we report on a significant step beyond this long-standing limit by combining newly developed soft x-ray Fresnel zone plate lenses with advanced precision in scanning control and careful optical design. With this approach, we achieve an image resolution of 7 nm. By combining this highly precise microscopy technique with the x-ray magnetic circular dichroism effect, we reveal dimensionality effects in an ensemble of interacting magnetic nanoparticles. Such effects are topical in current nanomagnetism research and highlight the opportunities of high-resolution soft x-ray microscopy in magnetism research and beyond. © 2020 Optical Society of America under the terms of the OSA Open Access Publishing Agreement

<https://doi.org/10.1364/OPTICA.399885>

1. INTRODUCTION

The use of x-rays to investigate the structure and properties of matter is an active field in scientific research [1]. X-ray microscopy and spectroscopy enable unique insights into condensed matter [2,3], magnetism [4,5], electronic materials [6,7], and biological specimens [8,9]. A multitude of scientific questions in the field of magnetism concerns length scales of some nanometers, such as ultra-small magnetic skyrmions for memory applications [10,11], or the nature of the coupling of adjacent magnetic nanoparticles and stacked thin films. In this context, x-ray-based methods with high resolving capabilities are ideally suited for microscopic applications that directly probe the magnetic properties of the sample under a wide range of excitations such as externally applied fields, current pulses, or radiofrequency waves. Another strong argument for x-ray microprobes is the fact that the perturbation that they induce to magnetic configurations is much less significant than, for

instance, is induced by the use of magnetic or electron microprobes [12–14].

Major achievements made in recent years have allowed the focusing of x-ray beams to spot sizes below 10 nm using mirrors [15], Fresnel zone plate (FZP) lenses [16,17], and multilayer Laue lenses [18,19]. These advances in x-ray optics have improved the spatial resolution of x-ray microscopy reliably to 10 nm [20,21]. In addition, other methods based on image reconstruction have reached imaging resolution well below 10 nm [7]. However, direct imaging at with better resolution remained difficult so far, due to the finesse of the overall instrument being limited by positioning precision and stability. Here we report on the first achievement of sub-10 nm microscopic resolution in real space for direct x-ray imaging. We demonstrate this in two scanning x-ray transmission microscopes (STXMs) at the PoLux [22] and HERMES [23] beamlines at the Swiss Light Source and Synchrotron Soleil, respectively.

2. HIGH-RESOLUTION SCANNING X-RAY MICROSCOPY

In scanning-based x-ray imaging, synchrotron radiation is usually focused using a FZP as a diffractive lens for x-rays [21–23]. Its resulting spot size under coherent illumination is comparable to the width of the outermost zone [24] of the lens. An order-selecting aperture (OSA) is positioned between the FZP and the specimen such that the desired focus order (usually the 1st) is able to pass while other diffraction orders, including the unfocused zero order beam, are blocked. The semitransparent sample is placed at the x-ray focus and raster-scanned while the intensity of the transmitted beam is measured as a function of position. The experimental setup for high-resolution STXM imaging is shown in Fig. 1. While the major constraint has previously been the nanofabrication of tightly focusing lenses [16,25–30], recent advances in lithography have provided us with a set of zone plates having outermost zone widths well below 10 nm [31]. For the presented experiments, we used FZP lenses with diameters of 100 μm at PolLux (or 240 μm at HERMES) and an outermost zone width of 8.8 nm that provided a focal length below 500 μm (or 1.2 mm) and a depth of focus less than ± 100 nm at a photon energy of 700 eV. This introduces extremely strict instrumental requirements. Therefore, the microscopes were carefully optimized to take full advantage of the sub-10 nm focusing, taking several factors into account such as the geometrical constraint of the small focal length, a high positioning accuracy of 3 nm RMS, and coherent illumination. In addition, the order-sorting aperture has been integrated onto the sample support for experiments with the iron nanoparticles (see Supplement 1).

In order to determine the spatial resolution of such a setup, we recorded test patterns with decreasing line widths of $w = 9$ nm, 8 nm, and 7 nm. These patterns consist of a periodic repetition of an iridium line, a line of silicon dioxide, a second iridium line, and a gap, each with the defined line width w and a height between 60 and 80 nm [Fig. 2(a), see Supplement 1]. Figure 2(b) shows a typical scanning electron micrograph of a test pattern with $w = 9$ nm. The x-ray transmission image of a similar area on the same sample is shown in Fig. 2(c). Note that the iridium lines (indicated with the

dotted line) now appear dark due to the high x-ray absorption compared to the lighter SiO_2 template structure and the gaps inside the rectangular iridium structures. The individual metal lines, as well as the spaces in between, are so clearly resolved that two collapsed lines (indicated with an arrow) can be distinguished from the regular pattern. We determined the spatial resolution using a two-dimensional Fourier shell correlation (FSC), i.e., a Fourier ring correlation, of two independent subsets of the image, shown in Fig. 2 (d). This approach is frequently used in the literature and allows for a comparison of our results to other x-ray microscopy studies in the literature [6,7,16,32,33], and yields a frequency cut-off at 0.14 nm^{-1} in Fourier space or 7.1 nm in real space. Note that other, less stringent criteria that are used in the literature would yield even lower numbers: the half-bit criterion [16] would result in 6.8 nm; the Rayleigh resolution at 11% contrast [7] is reached at 5.6 nm. Note that it is possible to improve the visibility further with a deconvolution using the calculated shape of the Airy disc of the focus spot [34]. In real space, we observe a loss of spatial resolution using test samples with $w < 7$ nm (see Supplement 1). Figure 2(e) shows a comparison of different test samples with 9, 8, and 7 nm line widths. To date, this is the highest spatial resolution demonstrated in direct x-ray microscopy.

3. MAGNETIC INTERACTION OF NANOPARTICLES

To demonstrate the capabilities of our lenses in microscopic applications with real samples which are not optimized for contrast and structural features as the test structures discussed above, we investigate a magnetic system with small nanostructures and high demand on contrast that is not accessible with synchrotron-based methods or other techniques so far [35]. We study the local response in an ensemble of magnetically interacting iron nanoparticles to an external magnetic field of 100 mT. The sample consists of isolated and agglomerated iron nanoparticles with bulk-like magnetization and a mean size of 12 nm. Nanoparticles in the agglomerates are in direct contact with each other and interact strongly via exchange in addition to dipolar interactions [36–40]. A 2–3 nm thick amorphous carbon layer was used to protect the

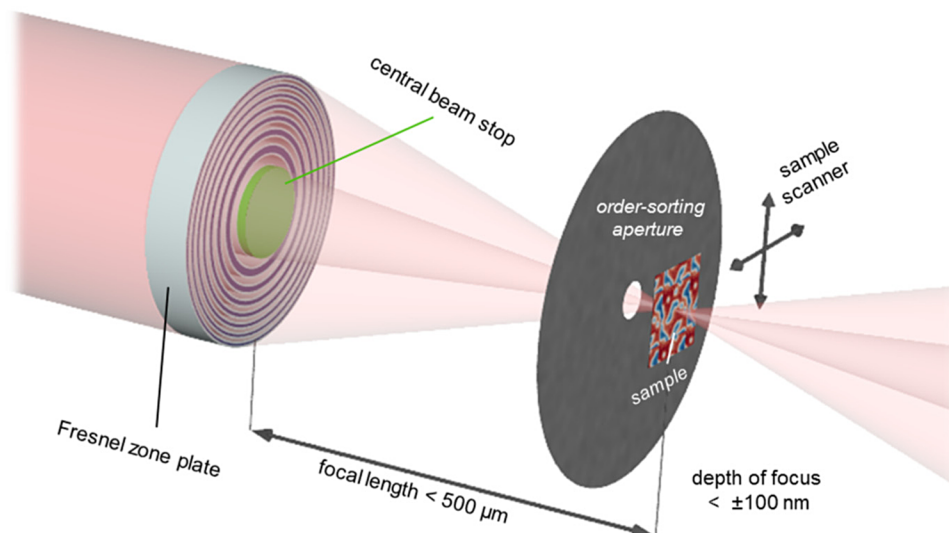


Fig. 1. Scanning x-ray transmission microscopy. Schematic illustration of the setup for high-resolution STXM. An opaque central beam stop and an aperture are used to select the first diffraction order of the zone plate. To achieve the demonstrated spatial resolution of 7 nm, a positioning accuracy of 3 nm and coherent illumination are required in addition to the Fresnel zone plate design.

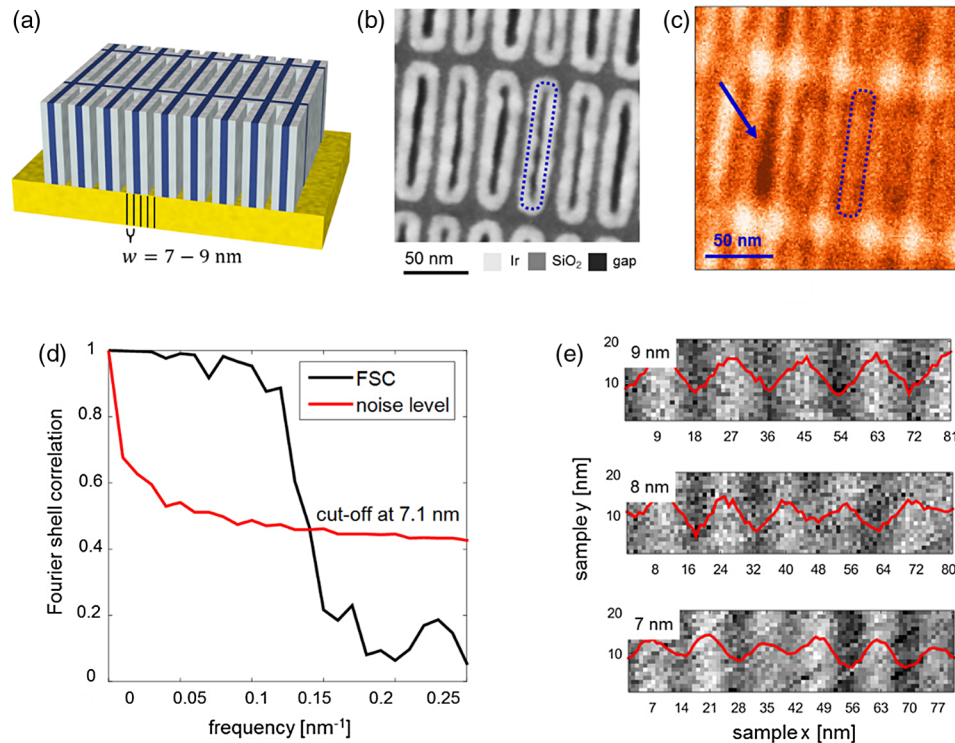


Fig. 2. High-resolution imaging of test patterns. (a) Model of typical test samples, consisting of repetitions of equidistant lines of iridium, silicon oxide, iridium, and a gap with $w = 9, 8, 7$ nm. (b) Scanning electron micrograph of a test pattern ($w = 9$ nm) used to evaluate the microscopic resolution. The material contrast is color-coded at the bottom. (c) Scanning transmission x-ray micrograph of a similar test structure (photon energy 700 eV, step size 1 nm). The arrow indicates two collapsed iridium lines; the blue-dotted line compares similar structures as recorded in scanning electron microscopy and STXM. (d) Two-dimensional Fourier shell correlation of (c). The frequency cutoff of the autocorrelation at the noise level is at 0.14 nm^{-1} , corresponding to 7.1 nm in real space. (e) Test patterns with $w = 9, 8,$ and 7 nm. Corresponding profiles of the average in vertical direction are overlaid on the images. The visibility of the patterns is 0.51%, 0.35%, and 0.31%, respectively.

sample against oxidation (see the [Supplement 1](#) for further details on sample preparation and properties). Ensembles of magnetic nanoparticles are of high interest in the field of nanomagnetism because they serve as model systems with complex magnetic interactions for the design of spintronic devices in two and three dimensions [14,41].

A scanning electron microscope image of the specimen presented in Fig. 3(a) reveals that the investigated sample exhibits a number of isolated nanoparticles and several nanoparticle agglomerates with complex morphology with features such as voids and edges. This is in contrast to typical resolution test samples that are merely designed to provide a high contrast, a high signal-to-noise ratio, and sharp features. Hence, this sample can serve as a benchmark for the potential and the remaining challenges of high-resolution scanning transmission x-ray microscopy in real samples; such an investigation would be impossible using currently available STXM setups, where the spot size is usually larger (15–20 nm) than the mean size of the nanoparticles. As a consequence, the low contrast would further smear out and the magnetic contrast might not be detectable.

The corresponding x-ray transmission micrographs [Fig. 3(b)] were recorded for both circular polarizations with the photon energy tuned to the Fe L_3 edge and perpendicular incidence. A comparison to the scanning electron microscope image in Fig. 3(a) shows that the isolated nanoparticles are not detected in the scanning x-ray transmission micrographs. In addition, voids and edges of the agglomerates are also not resolved. The achieved

resolution of the iron nanoparticles is clearly lower compared to values obtained for the test samples. Taking a closer look at the experimental conditions, we can identify the following differences between the two samples. (i) Although the absorption coefficient at the iron L_3 resonance is approx. 3 times higher ($\beta = 8 \cdot 10^{-3}$ for linear polarization [42]) than that of iridium at the same photon energy ($\beta = 2.5 \cdot 10^{-3}$ for linear polarization [43]), the test structures are more than 5 times higher than the thickness of the nanoparticles, resulting in a lower x-ray absorption of the nanoparticles. (ii) The iridium lines represent an almost ideal binary structure with well-defined transitions from high absorption (iridium) to low absorption (air or silicon oxide) within less than 1 nm, while the nanoparticles show a spherical shape [40] with smoother edges. The absorption profile close to the particle edges is therefore intrinsically less sharp and blurs the image contrast, especially when clusters of nanoparticles are scanned. (iii) For a full explanation of the lower resolution of the imaging system, we have further to take the lower available signal-to-noise ratio into account. When the nanoparticles are measured with circularly polarized light, the incoming flux drops by at least a factor of 2. In addition, we have to process two micrographs with opposite helicities of the circular polarization, resulting in added noise of two images recorded with low incident flux.

However, employing the Beer–Lambert law [44] with the optical constants of iron at the L_3 absorption edge [42], the local thickness of the large agglomerate can be retrieved as shown in Fig. 3(b). Together with the scanning electron microscope image,

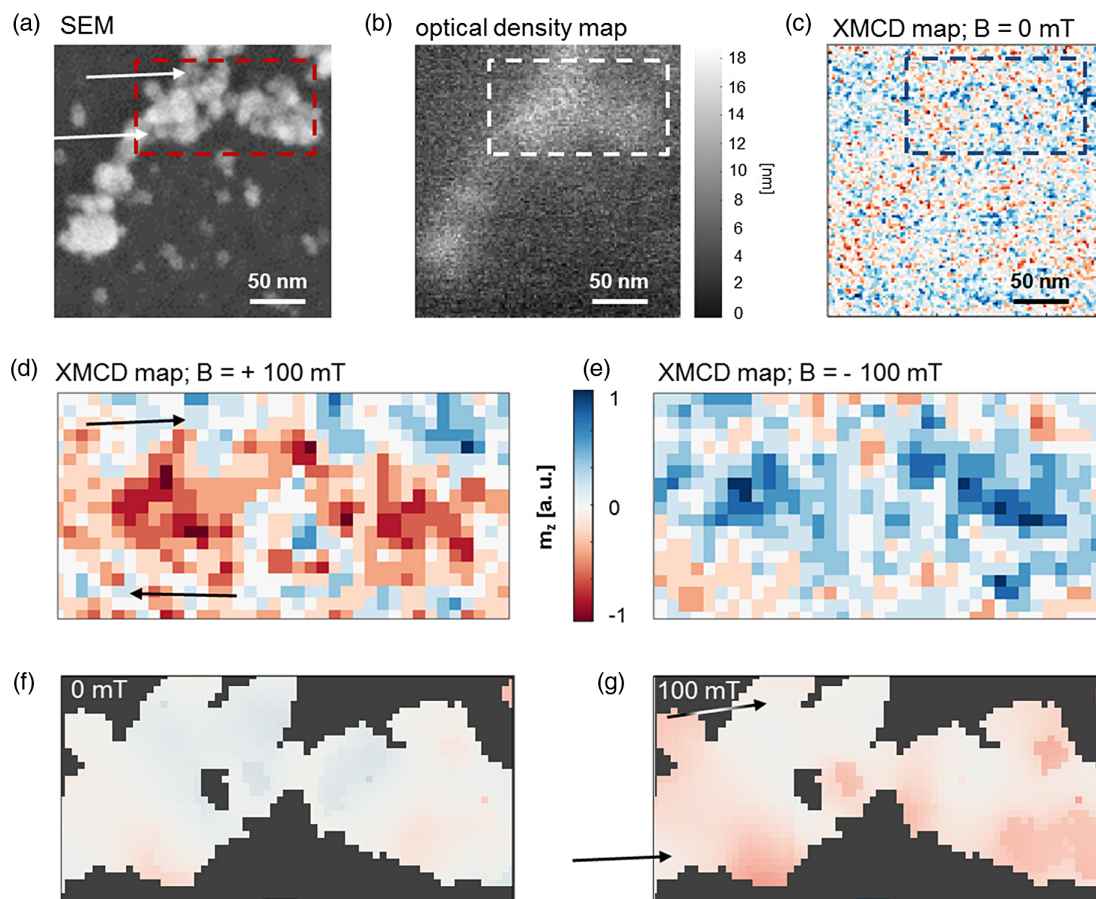


Fig. 3. Imaging of the out-of-plane magnetic component in iron nanoparticles. (a) Scanning electron micrograph of an agglomerate of iron nanoparticles. The size distribution of the individual particles reaches from approx. 5 nm to 20 nm. (b) Corresponding optical density map, calculated from the effective transmission of circularly polarized light with positive and negative chirality. Note that the optical density does not automatically coincide with the layer height. (c) Resulting XMCD map, showing the magnetic component out of the sample plane. (d), (e) XMCD images showing the part of the agglomerate that contains double layers with a differently oriented external magnetic field (± 100 mT). The region of the images is indicated with the dashed boxes in images (a)–(c). The arrows indicate parts where the inplane magnetization is stabilized by coupling interactions in contrast to regions, which exhibit out-of-plane magnetic contrast. (f) Micromagnetic simulation from a model derived from the SEM image of the nanoparticle agglomerates, revealing a vanishing out-of-plane magnetization due to strong inplane coupling via exchange and dipolar interactions at zero field. (g) Micromagnetic simulation of the same model for $+100$ mT applied out-of-plane. The data reveal stable inplane magnetized regions (see arrows) coexisting with out-of-plane magnetized regions, similar to the experimental data in (d).

the data reveal that the agglomerate consists mostly of a two-dimensional assembly of nanoparticles with a second, incomplete layer of particles in some areas. The magnetic contrast as a function of x-ray magnetic circular dichroism (XMCD), i.e., the difference of transmission using circularly polarized light with different helicities (see Supplement 1) without applying an external magnetic field, is shown in Fig. 3(c). The local absence of a magnetic contrast is consistent with a magnetic configuration where the magnetic moments of the agglomerated particles are oriented within the sample plane (i.e., perpendicular to \vec{k}) as has been observed in dipolar or exchange coupled nanomagnet arrays [41]. For the isolated nanoparticles either superparamagnetic or magnetically blocked states are expected [39]. The latter exhibit a random orientation of the magnetic moments, but their respective signals cannot be detected as stated above. Note that detecting isolated nanoparticles will require additional developments on the detector side.

Upon applying a magnetic field of ± 100 mT perpendicular to the sample plane, we notice that predominantly those regions

of the sample are magnetized that consist of at least two layers of iron nanoparticles, in contrast to the surrounding regions, which are mostly single-layered; see the regions highlighted by arrows in Figures 3(a) and 3(d). It has been previously demonstrated that an external magnetic field of a few mT is sufficient to magnetize the investigated iron nanoparticles at room temperature when they were well-isolated to prevent magnetic interparticle interactions [39]. While we cannot detect the signal of isolated nanoparticles, the absence of a magnetic contrast in the monolayer regions demonstrates remarkable magnetic interactions between the particles, which establish inplane coupling of the magnetic moments of the nanoparticles even when applying a field of 100 mT [some of these regions are highlighted with arrows in Figs. 3(a) and 3(d)]. The micrographs further disclose regions with nanoparticles in the second layer that can be locally magnetized and thus indicate a local destabilization of the inplane configuration.

In order to rationalize these observations, we performed micromagnetic simulations using a model derived from the sample morphology as seen in the scanning electron microscope (SEM)

and the optical density map. The simulations assumed bulk-like magnetic properties of iron (see the [Supplement 1](#)). Figure 3(f) shows the z-component (out-of-plane) of the magnetization of the simulated sample (normalized to the local thickness) in the absence of an external magnetic field. As experimentally observed, the magnetization lies mainly inplane due to the combined exchange and dipolar interactions. The application of a magnetic field of +100 mT results only locally in a noticeable out-of-plane magnetization, particularly in regions with the second layer on top, while the monolayer regions remain magnetized inplane, see Fig. 3(g). The simulations show that the observed local out-of-plane magnetization is caused by dipolar interactions due to structural features in the second layer, which possess lateral dimensions in the order of the thickness of the bottom layer. Further simulations with model systems show that even a single exchange-coupled nanoparticle can locally destabilize the inplane magnetization of a thin underlying film when placed in an external out-of-plane magnetic field with moderate magnitude (see [Supplement 1](#)). As a consequence, the actual magnetic configuration in complex samples as the present agglomerates depends critically on the detailed morphology, when extending a two-dimensional system into the third dimension.

4. OUTLOOK TO IMAGING OF ULTRA-SMALL MAGNETIC SYSTEMS

The high spatial resolution demonstrated in this study brings benefit to scientific issues that can be ideally addressed with x-ray imaging of magnetic components on the nanometer scale. A typical example for this is magnetic vortices or magnetic skyrmions [45]. The latter are topologically protected quasi-particles consisting of a magnetic domain surrounded by a chiral domain wall that cannot be continuously deformed into a ferromagnetic state without crossing a discontinuity in the magnetization [46]. This leads to various properties, such as an enhanced stability against annihilation at defects and the possibility to displace them electrically with low current densities [47]. Furthermore, magnetic skyrmions with sub-10 nm diameters can be stabilized in some materials, leading to the proposal to employ them as information carriers in novel high-density magnetic memory applications [47]. Up to now, the only established method that allowed for the investigation of such small, sub-10 nm magnetic skyrmions was scanning tunneling microscopy [48]. X-ray microscopic methods bear high potential as complementary imaging methods for ultra-small skyrmions. For instance, holographic imaging has demonstrated to have potential for measuring small skyrmions; however, its spatial resolution is limited by the reference holes that can be fabricated in the samples [10]. Another method to access magnetic structures on such small length scales is ptychography [49], yet sub-10 nm skyrmions have not yet been investigated with the method to the best of our knowledge.

The increased spatial resolution in soft x-ray microscopy in the present study now offers the possibility to investigate magnetic skyrmions with unprecedented precision. The minimum observable thickness with the setup installed at the PoLux beamline is on the order of 0.5–0.8 nm of perpendicularly magnetized cobalt [50]. Given the fact that this beamline operates at a bending magnet, we are optimistic that the minimum observable thickness for an undulator-based beamline will be even lower. However, not only the contrast from the investigated system limits the microscopic

resolution, as seen previously, but also the signal-to-noise ratio, or other effects, such as scattering at small particles. In this respect, the development and implementation of suitable, more sensitive detectors with quantum efficiencies close to 100% in the soft x-ray regime bears potential aiming for single-particle imaging.

Investigations on such systems are possible while still maintaining the flexibility of STXM regarding the sample environment, and the possibility to perform subnanosecond time-resolved studies. Implementation of a variable sample environment including cooling and various excitation sources will further enhance the capabilities toward dynamic measurements or the exploration of phase transitions.

5. CONCLUSIONS

In this study, we demonstrate x-ray microscopy with structural resolution well below 10 nm. We focused on scanning microscopy. In the future, we plan to extend the use of our zone plates to other microscopic methods, such as soft x-ray ptychography. The lateral resolution reached in this study offers a vast potential for research in nanomagnetism. Employing x-ray microscopy combines high sensitivity and direct, perturbation-free access to the magnetic component with imaging on the nanometer scale. For the implementation of our highly resolving Fresnel zone plates for routine operation, we identify two main challenges: first, the critical positioning control and stability of x-ray microscopes, and second, the quality of the incident x-ray beam. The importance of the mechanical precision becomes, for instance, obvious with the extremely small depth of focus below 100 nm at the sub-10 nm resolution level. The second challenge is related to the coherent photon flux at the used synchrotron sources, which limited the signal-to-noise level of the images that were obtained in this study. We expect strong improvements in this regard at the newly developed diffraction-limited x-ray sources [51] and possibly also at free-electron x-ray lasers. Their enhanced brilliance and coherence will unleash the full potential of highly resolving lenses for x-ray microscopy and pave the way for studying magnetism and other relevant materials at the nanometer length scale and with femtosecond resolution in the time domain.

Funding. Deutsche Forschungsgemeinschaft (SP 1775/1-1); Bundesministerium für Bildung und Forschung (05K16WED, 5K13WC3); FP7 People: Marie-Curie Actions (290605); H2020 Excellent Science (654360, 665095, 701647).

Acknowledgment. We gratefully acknowledge Istvan Mohacsi and Manuel Guizar-Sicairos for their Fourier-shell correlation code.

Disclosures. The authors declare no conflicts of interest.

See [Supplement 1](#) for supporting content.

REFERENCES AND NOTES

1. C. Jacobsen, *X-ray Microscopy* (Cambridge University, 2019).
2. V. Bisogni, S. Catalano, R. J. Green, M. Gibert, R. Scherwitzl, Y. Huang, V. N. Strocov, P. Zubko, S. Balandeh, J.-M. Triscone, G. Sawatzky, and T. Schmitt, "Ground-state oxygen holes and the metal-insulator transition in the negative charge-transfer rare-earth nickelates," *Nat. Commun.* **7**, 13017 (2016).

3. A. L. D. Kilcoyne, T. Tyliczszak, W. F. Steele, S. Fakra, P. Hitchcock, K. Franck, E. Anderson, B. Harteneck, E. G. Rightor, G. E. Mitchell, A. P. Hitchcock, L. Yang, T. Warwick, and H. Ade, "Interferometer-controlled scanning transmission x-ray microscopes at the advanced light source," *J. Synchrotron Rad.* **10**, 125–136 (2003).
4. C. Donnelly, M. Guizar-Sicairos, V. Scagnoli, S. Gliga, M. Holler, J. Raabe, and L. J. Heyderman, "Three-dimensional magnetization structures revealed with x-ray vector nanotomography," *Nature* **547**, 328–331 (2017).
5. G. Meier, M. Bolte, R. Eiselt, B. Krüger, D.-H. Kim, and P. Fischer, "Direct imaging of stochastic domain-wall motion driven by nanosecond current pulses," *Phys. Rev. Lett.* **98**, 187202 (2007).
6. M. Holler, M. Guizar-Sicairos, E. H. R. Tsai, R. Dinapoli, E. Müller, O. Bunk, J. Raabe, and G. Aeppli, "High-resolution non-destructive three-dimensional imaging of integrated circuits," *Nature* **543**, 402–406 (2017).
7. D. A. Shapiro, Y.-S. Yu, T. Tyliczszak, J. Cabana, R. Celestre, W. Chao, K. Kaznatcheev, A. L. D. Kilcoyne, F. Maia, S. Marchesini, Y. S. Meng, T. Warwick, L. L. Yang, and H. A. Padmore, "Chemical composition mapping with nanometre resolution by soft x-ray microscopy," *Nat. Photonics* **8**, 765–769 (2014).
8. S. M. Walker, D. A. Schwyn, R. Mokso, M. Wicklein, T. Müller, M. Doube, M. Stambanoni, H. G. Krapp, and G. K. Taylor, "In vivo time-resolved microtomography reveals the mechanics of the blowfly flight motor," *PLoS Biol.* **12**, e1001823 (2014).
9. M. Obst, J. J. Dynes, J. R. Lawrence, G. D. W. Swerhone, K. Benzerara, C. Karunakaran, K. Kaznatcheev, T. Tyliczszak, and A. P. Hitchcock, "Precipitation of amorphous CaCO₃ (aragonite-like) by cyanobacteria: a STXM study of the influence of EPS on the nucleation process," *Geochim. Cosmochim. Acta* **73**, 4180–4198 (2009).
10. L. Caretta, M. Mann, F. Büttner, K. Ueda, B. Pfau, C. M. Günther, P. Hessian, A. Churikova, C. Klose, M. Schneider, D. Engel, C. Marcus, D. Bono, K. Bagnschik, S. Eisebitt, and G. S. D. Beach, "Fast current-driven domain walls and small skyrmions in a compensated ferrimagnet," *Nat. Nano* **13**, 1154–1160 (2018).
11. A. Soumyanarayanan, M. Raju, A. L. Gonzalez Oyarce, A. K. C. Tan, M.-Y. Im, A. P. Petrović, P. Ho, K. H. Khoo, M. Tran, C. K. Gan, F. Ernult, and C. Panagopoulos, "Tunable room-temperature magnetic skyrmions in Ir/Fe/Co/Pt multilayers," *Nat. Mater.* **16**, 898–904 (2017).
12. C. Phatak, A. K. Petford-Long, and M. De Graef, "Recent advances in Lorentz microscopy," *Curr. Opin. Solid State Mater. Sci.* **20**, 107–114 (2016).
13. Y. Guang, I. Bykova, Y. Liu, G. Yu, E. Goering, M. Weigand, J. Gräfe, S. K. Kim, J. Zhang, H. Zhang, Z. Yan, C. Wan, J. Feng, X. Wang, C. Guo, H. Wei, Y. Peng, Y. Tserkovnyak, X. Han, and G. Schütz, "Creating zero-field skyrmions in exchange-biased multilayers through x-ray illumination," *Nat. Commun.* **11**, 949 (2020).
14. V. F. Puentes, P. Gorostiza, D. M. Aruguete, N. G. Bastus, and A. P. Alivisatos, "Collective behaviour in two-dimensional cobalt nanoparticle assemblies observed by magnetic force microscopy," *Nat. Mater.* **3**, 263–268 (2004).
15. H. Mimura, S. Handa, T. Kimura, H. Yumoto, D. Yamakawa, H. Yokoyama, S. Matsuyama, K. Inagaki, K. Yamamura, Y. Sano, K. Tamasaku, Y. Nishino, M. Yabashi, T. Ishikawa, and K. Yamauchi, "Breaking the 10 nm barrier in hard-x-ray focusing," *Nat. Phys.* **6**, 122–125 (2010).
16. I. Mohacsi, I. Vartiainen, B. Rösner, M. Guizar-Sicairos, V. A. Guzenko, I. McNulty, R. Winarski, M. V. Holt, and C. David, "Interlaced zone plate optics for hard x-ray imaging in the 10 nm range," *Sci. Rep.* **7**, 43624 (2017).
17. F. Döring, A. L. Robisch, C. Eberl, M. Osterhoff, A. Ruhlandt, T. Liese, F. Schlenkrich, S. Hoffmann, M. Bartels, T. Salditt, and H. U. Krebs, "Sub-5 nm hard x-ray point focusing by a combined Kirkpatrick-Baez mirror and multilayer zone plate," *Opt. Express* **21**, 19311–19323 (2013).
18. A. J. Morgan, M. Prasciolu, A. Andrejczuk, J. Krzywinski, A. Meents, D. Pennicard, H. Graafsma, A. Barty, R. J. Bean, M. Barthelmeß, D. Oberthuer, O. Yefanov, A. Aquila, H. N. Chapman, and S. Bajt, "High numerical aperture multilayer Laue lenses," *Sci. Rep.* **5**, 9892 (2015).
19. S. Bajt, M. Prasciolu, H. Fleckenstein, M. Domaracký, H. N. Chapman, A. J. Morgan, O. Yefanov, M. Messerschmidt, Y. Du, K. T. Murray, V. Mariani, M. Kuhn, S. Aplin, K. Pande, P. Villanueva-Perez, K. Stachnik, J. P. J. Chen, A. Andrejczuk, A. Meents, A. Burkhardt, D. Pennicard, X. Huang, H. Yan, E. Nazaretski, Y. S. Chu, and C. E. Hamm, "X-ray focusing with efficient high-NA multilayer Laue lenses," *Light Sci. Appl.* **7**, 17162 (2018).
20. S. Rehbein, S. Heim, P. Guttmann, S. Werner, and G. Schneider, "Ultra-high-resolution soft-x-ray microscopy with zone plates in high orders of diffraction," *Phys. Rev. Lett.* **103**, 110801 (2009).
21. W. Chao, P. Fischer, T. Tyliczszak, S. Rekawa, E. Anderson, and P. Naulleau, "Real space soft x-ray imaging at 10 nm spatial resolution," *Opt. Express* **20**, 9777–9783 (2012).
22. J. Raabe, G. Tzvetkov, U. Flechsig, M. Böge, A. Jaggi, B. Sarafimov, M. G. C. Vernooij, T. Huthwelker, H. Ade, D. Kilcoyne, T. Tyliczszak, R. H. Fink, and C. Quitmann, "PolLux: a new facility for soft x-ray spectro-microscopy at the Swiss Light Source," *Rev. Sci. Instrum.* **79**, 113704 (2008).
23. R. Belkhou, S. Stanescu, S. Swaraj, A. Besson, M. Ledoux, M. Hajlaoui, and D. Dalle, "HERMES: a soft x-ray beamline dedicated to x-ray microscopy," *J. Synchrotron Rad.* **22**, 968–979 (2015).
24. J. Vila-Comamala, K. Jefimovs, J. Raabe, T. Pilvi, R. H. Fink, M. Senoner, A. Maaßdorf, M. Ritala, and C. David, "Advanced thin film technology for ultrahigh resolution x-ray microscopy," *Ultramicroscopy* **109**, 1360–1364 (2009).
25. W. Chao, B. D. Harteneck, J. A. Liddle, E. H. Anderson, and D. T. Attwood, "Soft x-ray microscopy at a spatial resolution better than 15 nm," *Nature* **435**, 1210–1213 (2005).
26. W. Chao, J. Kim, S. Rekawa, P. Fischer, and E. H. Anderson, "Demonstration of 12 nm resolution Fresnel zone plate lens based soft x-ray microscopy," *Opt. Express* **17**, 17669–17677 (2009).
27. K. Jefimovs, J. Vila-Comamala, T. Pilvi, J. Raabe, M. Ritala, and C. David, "Zone-doubling technique to produce ultrahigh-resolution x-ray optics," *Phys. Rev. Lett.* **99**, 264801 (2007).
28. J. Vila-Comamala, A. Diaz, M. Guizar-Sicairos, A. Mantion, C. M. Kewish, A. Menzel, O. Bunk, and C. David, "Characterization of high-resolution diffractive x-ray optics by ptychographic coherent diffractive imaging," *Opt. Express* **19**, 21333–21344 (2011).
29. J. Vila-Comamala, S. Gorelick, E. Färm, C. M. Kewish, A. Diaz, R. Barrett, V. A. Guzenko, M. Ritala, and C. David, "Ultra-high resolution zone-doubled diffractive x-ray optics for the multi-keV regime," *Opt. Express* **19**, 175–184 (2011).
30. S. Rehbein, A. Lyon, R. Leung, M. Feser, and G. Schneider, "Near field stacking of zone plates for reduction of their effective zone period," *Opt. Express* **23**, 11063–11072 (2015).
31. B. Rösner, F. Koch, F. Döring, J. Bosgra, V. A. Guzenko, E. Kirk, M. Meyer, J. L. Ornelas, R. H. Fink, S. Stanescu, S. Swaraj, R. Belkhou, B. Watts, J. Raabe, and C. David, "Exploiting atomic layer deposition for fabricating sub-10nm x-ray lenses," *Microelectron. Eng.* **191**, 91–96 (2018).
32. M. van Heel and M. Schatz, "Fourier shell correlation threshold criteria," *J. Struct. Biol.* **151**, 250–262 (2005).
33. M. Holler, A. Diaz, M. Guizar-Sicairos, P. Karvinen, E. Färm, E. Härkönen, M. Ritala, A. Menzel, J. Raabe, and O. Bunk, "X-ray ptychographic computed tomography at 16 nm isotropic 3D resolution," *Sci. Rep.* **4**, 3857 (2014).
34. J. L. Ornelas, B. Rösner, A. Späth, and R. H. Fink, "STXMdeconv—a MATLAB script for the deconvolution of STXM images," *Microsc. Microanal.* **24**, 120–121 (2018).
35. We note that XPEEM has been successfully used in the past to probe the magnetism of individual iron nanoparticles, which is possible due the surface sensitivity of the secondary detection [A. F. Rodríguez *et al.*, *Phys. Rev. Lett.* **104** (12), 127201 (2010), Kronast *et al.* *Nano Lett.* **2011**, **11**, 4, 1710–1715]. For this method, it is required that the nanoparticles are sufficiently separated (typically by 100–200 nm) to isolate their individual signals, since the actual spatial resolution of XPEEM is typically limited to 50–100 nm [A. Scholl, M. A. Marcus, A. Doran, J. R. Nasiatka, A. T. Young, A. A., MacDowell, R. Streubel, N. Kent, J. Feng, W. Wan, and H. A. Padmore. *Ultramicroscopy*, **188**:77, 2018]. Further, the application of external magnetic fields is usually limited to about 10 mT in XPEEM imaging. Studying local magnetic properties within agglomerates with the spatial resolution presented here is therefore only possible in STXM.
36. J. Bansmann and A. Kleibert, "Magnetism of mass-filtered nanoparticles on ferromagnetic supports," *Appl. Phys. A* **80**, 957–964 (2005).
37. A. Kleibert, J. Passig, K. H. Meiwes-Broer, M. Getzlaff, and J. Bansmann, "Structure and magnetic moments of mass-filtered deposited nanoparticles," *J. Appl. Phys.* **101**, 114318 (2007).

38. A. Kleibert, K. H. Meiwes-Broer, and J. Bansmann, "Size-dependent magnetic spin and orbital moments of Fe nanoparticles deposited onto Co/W(110)," *Phys. Rev. B* **79**, 125423 (2009).
39. A. Balan, P. M. Derlet, A. F. Rodríguez, J. Bansmann, R. Yanes, U. Nowak, A. Kleibert, and F. Nolting, "Direct observation of magnetic metastability in individual iron nanoparticles," *Phys. Rev. Lett.* **112**, 107201 (2014).
40. A. Kleibert, A. Balan, R. Yanes, P. M. Derlet, C. A. F. Vaz, M. Timm, A. Fraile Rodríguez, A. Béché, J. Verbeeck, R. S. Dhaka, M. Radovic, U. Nowak, and F. Nolting, "Direct observation of enhanced magnetism in individual size- and shape-selected $3d$ transition metal nanoparticles," *Phys. Rev. B* **95**, 195404 (2017).
41. M. Varón, M. Beleggia, T. Kasama, R. J. Harrison, R. E. Dunin-Borkowski, V. F. Puentes, and C. Frandsen, "Dipolar magnetism in ordered and disordered low-dimensional nanoparticle assemblies," *Sci. Rep.* **3**, 1234 (2013).
42. J. B. Kortright and S.-K. Kim, "Resonant magneto-optical properties of Fe near its $2p$ levels: measurement and applications," *Phys. Rev. B* **62**, 12216–12228 (2000).
43. B. L. Henke, E. M. Gullikson, and J. C. Davis, "X-ray interactions: photoabsorption, scattering, transmission, and reflection at $E = 50$ – $30,000$ eV, $Z = 1$ – 92 ," *At. Data Nucl. Data Tables* **54**, 181–342 (1993).
44. A. Beer, "Bestimmung der absorption des rothen Lichtes in farbigen Flüssigkeiten," *Ann. Phys.* **162**, 78–88 (1852).
45. F. Büttner, I. Lemesh, and G. S. D. Beach, "Theory of isolated magnetic skyrmions: from fundamentals to room temperature applications," *Sci. Rep.* **8**, 4464 (2018).
46. N. Nagaosa and Y. Tokura, "Topological properties and dynamics of magnetic skyrmions," *Nat. Nano* **8**, 899–911 (2013).
47. A. Fert, V. Cros, and J. Sampaio, "Skyrmions on the track," *Nat. Nano* **8**, 152–156 (2013).
48. P.-J. Hsu, L. Rózsa, A. Finco, L. Schmidt, K. Palotás, E. Vedmedenko, L. Udvardi, L. Szunyogh, A. Kubetzka, K. von Bergmann, and R. Wiesendanger, "Inducing skyrmions in ultrathin Fe films by hydrogen exposure," *Nat. Commun.* **9**, 1571 (2018).
49. W. Li, I. Bykova, S. Zhang, G. Yu, R. Tomasello, M. Carpentieri, Y. Liu, Y. Guang, J. Gräfe, M. Weigand, D. M. Burn, G. van der Laan, T. Hesjedal, Z. Yan, J. Feng, C. Wan, J. Wei, X. Wang, X. Zhang, H. Xu, C. Guo, H. Wei, G. Finocchio, X. Han, and G. Schütz, "Anatomy of skyrmionic textures in magnetic multilayers," *Adv. Mater.* **31**, 1807683 (2019).
50. M. Baumgartner, K. Garello, J. Mendil, C. O. Avci, E. Grimaldi, C. Murer, J. Feng, M. Gabureac, C. Stamm, Y. Acremann, S. Finizio, S. Wintz, J. Raabe, and P. Gambardella, "Spatially and time-resolved magnetization dynamics driven by spin-orbit torques," *Nat. Nanotechnol.* **12**, 980–986 (2017).
51. M. Eriksson, J. F. van der Veen, and C. Quitmann, "Diffraction-limited storage rings—a window to the science of tomorrow," *J. Synchrotron Rad.* **21**, 837–842 (2014).